GDCh Research Article Angewandte International Edition Chemie www.angewandte.org

How to cite: Angew. Chem. Int. Ed. 2024, e202407881
doi.org/10.1002/anie.202407881

Zinc Batteries Hot Paper

Mass Transfer Limitation within Molecular Crowding Electrolyte Reorienting (100) and (101) Texture for Dendrite-Free Zinc Metal Batteries

*Ziqing Wang, Jiaao Wang, Kenta Kawashima, Zonghang Liu, Graeme Henkelman, and C. Buddie Mullins**

Abstract: Aqueous zinc metal batteries are emerging as a promising alternative for energy storage due to their high safety and low cost. However, their development is hindered by the formation of Zn dendrites and side reactions. Herein, a macromolecular crowding electrolyte (MCE40) is prepared by incorporating polyvinylpyrrolidone (PVP) into the aqueous solutions, exhibiting an enlarged electrochemical stability window and anti-freezing properties. Notably, through electrochemical measurements and characterizations, it is discovered that the mass transfer limitation near the electrode surface within the MCE40 electrolyte inhibits the (002) facets. This leads to the crystallographic reorientation of Zn deposition to expose the (100) and (101) textures, which undergo a "nucleation-merge-growth" process to form a uniform and compact Zn deposition. Consequently, the MCE40 enables highly reversible and stable Zn plating/stripping in Zn/Cu half cells over 600 cycles and in Zn/Zn symmetric cells for over 3000 hours at 1.0 mA cm^{-2}. Furthermore, $Na_{0.33}V_2O_5$/Zn and α-MnO_2/Zn full cells display promising capacity and sustained stability over 500 cycles at room and sub-zero temperatures. This study highlights a novel electrochemical mechanism for achieving preferential Zn deposition, introducing a unique strategy for fabricating dendrite-free zinc metal batteries.

[*] Z. Wang, J. Wang, K. Kawashima, Prof. G. Henkelman, Prof. C. B. Mullins
Department of Chemistry
The University of Texas at Austin
Austin, TX 78712, United States
E-mail: mullins@che.utexas.edu

J. Wang, Prof. G. Henkelman
Oden Institute for Computational Engineering and Sciences
The University of Texas at Austin
Austin, TX 78712, United States

Z. Liu
School of Science and Engineering, Shenzhen Key Laboratory of Functional Aggregate Materials
The Chinese University of Hong Kong
Shenzhen, Guangdong, 518172, P. R. China

Prof. C. B. Mullins
McKetta Department of Chemical Engineering
The University of Texas at Austin
Austin, TX 78712, United States

Introduction

Aqueous zinc metal batteries (AZMBs) have been considered a promising option for large-scale energy storage due to their high safety and low cost.[1] However, several challenges, such as narrow electrochemical stability windows induced by water splitting, rampant Zn dendrite growth on the anode, and severe dissolution of the cathode in aqueous electrolytes, significantly restrict the cycling stability and reversibility of AZMBs.[2] Notably, one of the primary obstacles to developing a stable Zn anode is uncontrollable dendrite evolution at the electrode-electrolyte interface.[3] This dendrite growth is responsible for short circuits occurring in the batteries. Therefore, it is effective to modify the electrode-electrolyte interface to regulate Zn deposition features and suppress the formation of Zn dendrites.

It has been reported that controlling the crystallography of Zn deposited on the anode efficiently achieves uniform Zn deposition.[4] Specific Zn deposition can eliminate the crystallographic heterogeneities. Hexagonal Zn metal has three primary crystal planes [i.e., (002), (100), and (101)], out of which the (002) facet has been frequently discussed due to its low hydrogen evolution reaction (HER) activity, anti-corrosion stability, low surface energy, and planar morphology.[4e,5] However, the high stability of the (002) plane due to its low surface energy indicates inferior chemical activity and slow reaction kinetics, which is detrimental to Zn plating/stripping. In contrast, the other two facets with higher surface energy exhibit faster deposition kinetics.[6] However, accumulating (100) and (101) facets tends to cause a tip effect and facilitate dendrite formation, which is undesirable.[7] Therefore, the controlled deposition of (100) and (101) planes has not been given much attention. Liu et al. constructed a highly textured (101) Zn substrate via an annealing process, which allowed for the epitaxial growth of the (101) facet in the deposited Zn.[8] Additionally, Wang et al. and Zhu et al. were able to achieve (100) plane-dominated Zn deposition by introducing small amounts of serine ($C_3H_7NO_3$) and disodium lauryl phosphate, respectively, to shield the growth of (002) facets.[6,9] The vertical and compact distribution of (100) and (101) planes can effectively enhance the homogeneity. Accordingly, it is necessary to develop new approaches for reorienting the Zn crystallography to achieve homogeneous Zn (100) and (101) facets deposition.

The process of Zn deposition involves two main steps. Initially, Zn^{2+} ions are transported to the electrode, which acts as a source of electrons. Then, the transported Zn^{2+} ions are reduced at the electrode surface as Zn metal.[10] The transport of Zn^{2+} ions to the electrode surface is necessary, as it is intricately linked with the interfacial reaction kinetics, ultimately influencing the Zn deposition. When the reaction rate at the metal surface is limited, fast Zn^{2+} ion transportation can continuously provide ions to supplement the ions consumed by the interfacial reactions. In this case, Zn metal deposition is only related to the electron transmission rate in the electrode. However, the reaction kinetics on the electrode surface is always faster than ion transportation from the electrolyte to the electrode. Therefore, the mass transfer in the electrolyte is the rate-determine step for Zn metal deposition. When the consumption of Zn^{2+} ions exceeds the rate of ion transport, an ion depletion zone lacking Zn^{2+} ions is formed on the electrode surface.[11] The physicochemical properties of this layer are closely related to the morphology and crystallography of Zn deposition. Zheng et al. discovered that the reorientation of Zn crystallography from a parallel (002) plane to a vertical (100) plane could overcome the ion depletion caused by mass transfer limitation.[12] This is because the vertically oriented Zn metal is more likely to contact the Zn^{2+} ions outside of the depletion zone to facilitate Zn deposition than the parallel stacked Zn. Therefore, creating a Zn^{2+} ion depletion zone through mass transfer limitation can effectively control the crystalline orientation of Zn metal on the substrate.

Herein, we describe the design of a macromolecular crowding electrolyte (MCE) by introducing polyvinylpyrrolidone (PVP) into a $Zn(ClO_4)_2$-based aqueous solution. In this electrolyte, PVP molecules form strong hydrogen bonds with H_2O molecules, significantly suppressing the water activity and thereby enlarging the electrochemical stability window. Meanwhile, progressive nucleation in this MCE enables highly reversible Zn plating/stripping and exhibits superior Coulombic efficiency (CE). Notably, the analyses of the evolution in Zn deposition morphology and crystallinity demonstrate the crystallographic reorientation of Zn deposition into (101) and (100) facets. More importantly, electrochemical tests using a rotating disc electrode (RDE) and a three-electrode system highlight the significant mass transfer limitation in the MCE, which is the dominant factor for the reoriented crystallinity. The small grains containing (101) and (100) planes merge with each other and eventually grow into a close-packed structure with uniform morphology. As a result of suppressed water activity and favorable Zn deposition, Zn/Zn symmetric cells can stably cycle for over 3000 hours at various current densities (0.5, 1.0, and 5.0 $mA\,cm^{-2}$). Furthermore, leveraging these advantages, $Na_{0.33}V_2O_5$ (NaVO)/Zn and α-MnO_2 (MnO_2)/Zn full cells exhibit promising cycling stability and capacity across a wide temperature range from −20 to 50 °C. This work presents an approach to reorienting the crystallography of deposited Zn, facilitating highly uniform dendrite-free Zn anodes.

Results and Discussion

Structure and Coordination Environment of Electrolytes

The macromolecular crowding phenomenon is a common effect in living cells describing the altered properties of water molecules within a solution.[13] Due to the strong hydrogen bonds between macromolecules and water molecules, water activity is significantly suppressed. Inspired by this phenomenon, PVP, a safe and non-toxic polymer,[14] was employed as the macromolecule to prepare macromolecular MCE. Previous works also introduced PVP as an additive to aqueous electrolytes, whereas the concentrations were very low.[15] In this work, high-content PVP with various weight ratios (i.e., 10, 20, 30, 40, and 50 %) were incorporated into 2 $mol\,kg^{-1}{}_{solvent}$ (m) $Zn(ClO_4)_2$ aqueous solutions to yield MCE10, MCE20, MCE30, MCE40, and MCE50, respectively. For comparison, 2 m $Zn(ClO_4)_2$ aqueous electrolyte (denoted as AqE) was selected.

Fourier transform infrared spectroscopy (FTIR) characterization demonstrates the chemical environment change brought about by varying amounts of PVP (Figure S1). As depicted in Figure 1a, all the electrolytes exhibit a broad band between 2800 and 3800 cm^{-1}, corresponding to the O–H stretching vibration in H_2O molecules. It is obvious that the peak intensities gradually decrease with the increase of PVP content in the solutions. Furthermore, the deconvoluted results in Figure S2 demonstrate the increased amount of non-H-bond and weak H-bond water molecules, indicating reduced H-bond networking interactions between H_2O molecules.[16] Moreover, the O–H bending vibration in Figure 1b demonstrates a blueshift with the increase of PVP molecules due to hydrogen bonds between PVP and H_2O molecules.[17] Compared to PVP powder, the C=O vibrations in MCEs exhibit a blueshift to higher wavenumbers, confirming that the O from the C=O group coordinates with H from H_2O through hydrogen bonds (Figure 1c).[18]

To verify the hydrogen bonding change, ^1H nuclear magnetic resonance (NMR) measurements of the electrolytes were conducted (Figure 1d). The peaks in the ^1H NMR shifted downfield with increasing PVP content, suggesting the de-shielding effect of the H in H_2O molecules and the formation of hydrogen bonds between H_2O and PVP.[19] Due to the strong intermolecular interactions between PVP and H_2O, the activity of free water has been significantly suppressed, which was confirmed by an evaporation experiment (Figure S3). The discrepancy in mass retention demonstrates that the high concentration of PVP effectively reduces the activity of free water molecules. Linear sweep voltammetry (LSV) results in Figure S4 illustrate that as the PVP content increases, the onset potentials for HER and oxygen evolution reaction (OER) shift toward more negative and positive values, respectively, indicating that the overall water splitting is decreased due to restricted free water activity. However, given that the redox potentials for Zn^{2+}/Zn and H^+/H_2 are very close, it is challenging to distinguish the HER onset potentials by using a Zn-based electrolyte. Therefore, 2 m $LiClO_4$ electrolytes with different PVP contents were employed to measure the LSV. As

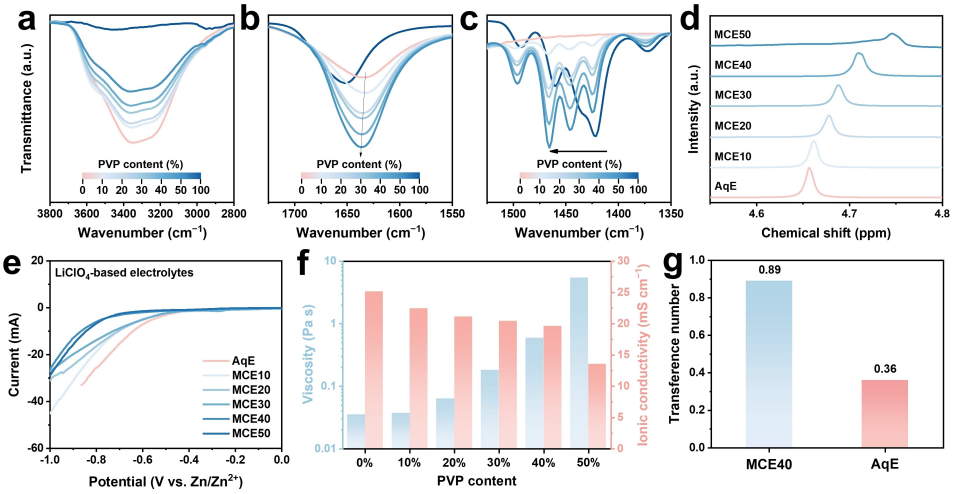

Figure 1. Characterization results of different electrolytes. (a-c) FTIR spectra of AqE, MCEs, and PVP. (d) ^{1}H NMR spectra of AqE and MCEs. (e) LSV curves of 2 m $LiClO_4$-based AqE and MCEs at the cathodic sweep. (f) Viscosity and ionic conductivity of AqE and MCEs. (g) Zn^{2+} ion transference numbers of AqE and MCE40.

shown in Figure 1e, the onset potentials for HER in MCE40 and MCE50 exhibit more negative values than the other four electrolytes, suggesting that the HER was suppressed. Similarly, the onset potential of OER in MCE40 and MCE50 is higher than in the other four electrolytes (Figure S5). The above results indicate that the electrochemical stability windows were enlarged in MCE40 and MCE50. Density functional theory (DFT) calculations provide theoretical evidence for the tuned intermolecular interactions. The hydrogen bonds between PVP and H_2O are two times stronger than those between H_2O molecules, indicating that H_2O tends to coordinate with PVP instead of another H_2O in the MCEs (Figure S6).

The physicochemical properties of AqE and MCEs were evaluated and compared. A flammability test indicates that despite adding large amounts of PVP, MCEs are non-flammable and exhibit promising safety (Figure S7). Considering PVP is a long-chain polymer, increasing its content in the electrolyte resulted in gradually increased viscosities and decreased ionic conductivities (Figure 1f, S8, and S9). It is worth noting that when the PVP content exceeds 40 %, a significant drop in ionic conductivity and an increase in viscosity are observed, which makes MCE50 unsuitable for practical use in batteries. The inferior physicochemical properties of MCE50 are also investigated via wettability tests. As shown in Figure S10 and S11, MCEs10–40 exhibit similar wettability to Zn electrodes and glass fiber separators as AqE, while MCE50 shows worse wettability on both Zn electrode and separator, confirming its less favorable performance in battery application.

Cycling tests were carried out using Zn/Zn symmetric cells at variable current densities to gain more insights into the impact of AqE and MCEs on electrochemical performance. Figure S12 shows that the battery within AqE has the shortest cycling life, only 60 hours before experiencing a short circuit. Additionally, MCE50 also exhibits short cycling, likely due to its high viscosity and low ionic conductivities. In contrast, MCEs10–40 demonstrate reversible cycling at current densities ranging from 0.5 to 5.0 mA cm^{-2}, indicating that the addition of a proper amount of PVP can facilitate reversible Zn plating/stripping. Notably, after cycling at 5.0 mA cm^{-2}, MCE40 shows the longest cycling performance, lasting over 800 hours at 0.5 mA cm^{-2}. Based on the physicochemical properties and cycling stability results, MCE40 was selected as the optimized electrolyte for further tests and measurements in this work. Even though MCE40 has inferior ionic conductivity and viscosity compared to AqE, MCE40 exhibits a Zn^{2+} transference number twice as high as AqE's, representing higher efficiency for Zn^{2+} ion transport (Figure 1g and S13). This enhanced transference number can be ascribed to the carbonyl and pyrrole groups within PVP molecules, which interact with Zn^{2+} ions, allowing them to move rapidly along the polymer backbone.[15a]

DFT-molecular dynamics (DFT-MD) simulations were employed to explore the solvation structures of Zn^{2+} within AqE and MCE40. Figure S14a and S14b illustrate that the presence of PVP molecules in the Zn^{2+} solvation structure of MCE40 is minimal. This scarcity is attributed to the large size of PVP molecules, which induces the steric hindrance effect, making it hard to solvate Zn^{2+}. Additionally, with the introduction of PVP molecules into the MCE40, a decrease in H_2O content and an increase in ClO_4^- ions within the first solvation sheath can be observed, demonstrating an anion-rich solvation structure of Zn^{2+} in MCE40 (Figure S14c and S14d).

Investigation of Zn Plating/Stripping Behavior

The behavior of Zn plating and stripping on the Cu foils was evaluated in the Zn/Cu half cells using different electrochemical tests. Cyclic voltammetry (CV) measurements at 0.2 mV s^{-1} were conducted in the Zn/Cu half cells to

determine the reaction kinetics. As shown in Figure S15a, the CV curves of both electrolytes display a broad peak at a similar position, whereas a more negative overpotential of −0.21 V for the battery can be observed in MCE40, suggesting a smaller degree of Zn nucleation and suppressed HER, which is also confirmed by the nucleation overpotential-time profile (Figure S16). Additionally, after ten CV cycles, the battery using MCE40 still exhibits a CV curve similar to the first cycle, representing that Zn plating/stripping is highly reversible with MCE40 (Figure S15b). In contrast, the features of water splitting can be observed in the 10th cycle of the battery in AqE. To further evaluate the plating/stripping reversibility and stability of each electrolyte, the Zn/Cu cells were cycled under a current density of 1.0 mA cm^{-2} to reach an areal capacity of 0.5 mAh cm^{-2} (Figure 2a). Due to the reversible Zn plating/stripping within the MCE40, the Zn/Cu cell with MCE40 exhibits a high CE of 99.4 % over 600 cycles. However, the Zn/Cu cell with AqE only maintained a CE of 96.4 % for 300 cycles with obvious fluctuations (Figure S17), illustrating the occurrence of side reactions.

Zn nucleation and deposition behaviors were further evaluated using the chronoamperometry (CA) method, in which we recorded the time-dependent current change under a constant overpotential of −200 mV. As shown in Figure 2b, both curves exhibit a short-time current increase followed by a current decrease after the peak current. The current increase represents the two-dimensional nucleation and growth of Zn nuclei.[20] After the peak current, the current decline in both curves corresponds to the continuous nucleation process coupled with subsequent Zn growth. Although both curves exhibit similar peak currents, the nucleation and Zn growth behaviors in these electrolytes are fundamentally different. Based on the calculation and simulation results presented in Figure 2c, the nucleation in MCE40 follows a progressive pattern, while it is instantaneous in AqE.[21] The progressive nucleation in MCE40 demonstrates the continuous formation of smaller Zn nuclei with a more uniform distribution than AqE (Figure S18). On the contrary, the instantaneous nucleation leads to larger Zn nuclei accumulated on the nucleation sites on the electrode surface, which can eventually grow into a Zn dendrite. In addition to the discrepancy in nucleation modes, the Zn growth behaviors in both electrolytes are also different. As for the Zn growth in MCE40, Zn^{2+} ions tend to deposit where they adsorb without diffusing to other existing Zn spots. Since there is no Zn^{2+} diffusion, this process needs little energy, thereby consistent with the decreased current.[22] In contrast, after a 200-second current decrease, a continuous current increase occurs until 600 seconds in AqE. This process represents 2D Zn growth, where Zn^{2+} ions diffuse on the electrode surface for energy-favorable sites (i.e., existing Zn nuclei) to deposit, eventually evolving into Zn dendrites.[23] The increased current provides extra energy to drive this process. Meanwhile, the enlarged surface area due to the formation of Zn dendrites in AqE also contributes to the increased current.

The Cu foils after Zn deposition were characterized through scanning electron microscope (SEM) and X-ray diffraction (XRD) techniques. The SEM and 3D topography images of the Cu foil cycled in the MCE40 emphasize a uniform surface without the formation of Zn dendrites (Figure 2d and S19). However, a dendrite with a diameter of 100 μm can be found in the SEM and 3D topography images of the Cu foil in AqE, confirming that the parasitic reactions and instantaneous nucleation lead to the formation of Zn dendrites in AqE (Figure 2d and S19). As well as the difference in morphology, the crystallography of deposited

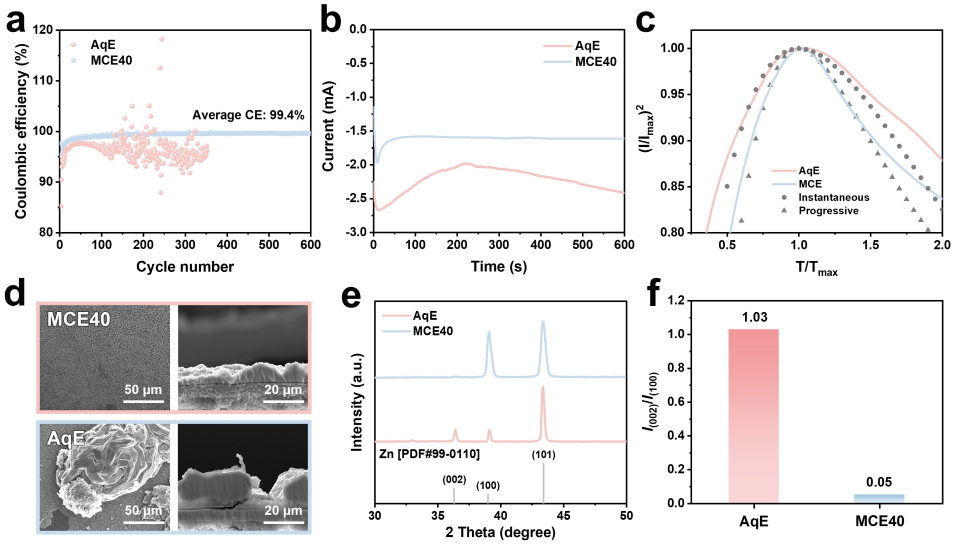

Figure 2. Electrochemical performance of AqE and MCE40 in Zn/Cu half cells. (a) CEs of Zn/Cu half cells under a current density of 1.0 mA cm^{-2} to a capacity of 0.5 mAh cm^{-2}. (b) Current-time profiles of both electrolytes under a CA measurement at an overpotential of −200 mV in Zn/Cu half cells. (c) Theoretical and experimental dimensionless curves for instantaneous and progressive nucleation derived from CA results. (d) SEM images and (e) XRD patterns of Zn deposited Cu foils after CA tests. (f) Peak intensity ratios between (002) and (100) facets derived from XRD patterns.

Zn measured by XRD in both electrolytes also shows different trends (Figure 2e). The Zn deposited in AqE exhibits three main diffraction peaks. However, in the case of MCE40, the (002) diffraction peak intensity disappears, and the intensity of the (100) facet is boosted. These features demonstrate that the MCE40 can reorient the crystallography of Zn deposition. Figure 2f illustrates that the Zn metal is almost vertically aligned on the Cu foil surface in MCE40, indicating that the exposure of the (002) plane has been suppressed.

Electrochemical Performance of Zn/Zn Symmetric Cells

The electrochemical performance of AqE and MCE40 was assessed in Zn/Zn symmetric cells by analyzing potential-time profiles of Zn plating/stripping at different current densities and areal capacities. As seen in Figure 3a, the Zn/Zn symmetric cell in MCE40 at 0.5 mA cm^{-2} displays stable cycling for over 2000 hours without any significant overpotential increase. In contrast, the Zn/Zn cell in AqE experiences a short circuit that occurs after ~200-hour cycling due to the formation of Zn dendrites. Similarly, the Zn/Zn symmetric cell in AqE undergoes a short circuit after 100 hours at a current density of 1.0 mA cm^{-2}, while the one in MCE40 still exhibits reversible and stable cycling for over 3000 hours (Figure 3b). The stability of MCE40 in symmetric cells is further confirmed by its cycling performance at high current densities at 5.0 and 7.5 mA cm^{-2} to capacities of 5.0, 10.0, and 15.0 mAh cm^{-2} (Figure S20). Even under high current densities and areal capacities, the Zn/Zn symmetric cells in MCE40 can still stably cycle for at least 400 hours without failure, while the ones in AqE experienced short circuits. Optical Zn/Zn symmetric cells in both electrolytes provide visible evidence of the formation of Zn dendrites in AqE and uniform plating in MCE40. As depicted in Figure 3c, small Zn dendrites formed on the Zn surface after 6 minutes in AqE, which grew bigger after depositing 9 minutes. In contrast, MCE40 facilitated a homogeneous Zn deposition, keeping the surface smooth and uniform even after a 9-minute deposition. Similar results can be observed in optical cells under a higher current density and areal capacity (Figure S21). The non-uniformly deposited surface appeared after 8 minutes in AqE, which grew into big dendrites after 16 minutes. However, the Zn surface remained homogeneous without any dendrite formation for 20 minutes, confirming that the existence of PVP can effectively smooth the surface and suppress the dendrites. Further, SEM and 3D topography images of Zn electrodes after cycling provide evidence for the formation of Zn dendrites in AqE and homogeneous Zn deposition in MCE40 (Figure 3d, S22, and S23). Notably, the morphology of deposited Zn in MCE40 is distinctive. Figure 3d and S24 show that the deposited Zn exhibits a vertically oriented arrangement with a compacted structure, which looks like vertical blades stacked up. XRD measurements were conducted to analyze the crystalline structure of deposited Zn (Figure 3e). Consistent with previous XRD results on

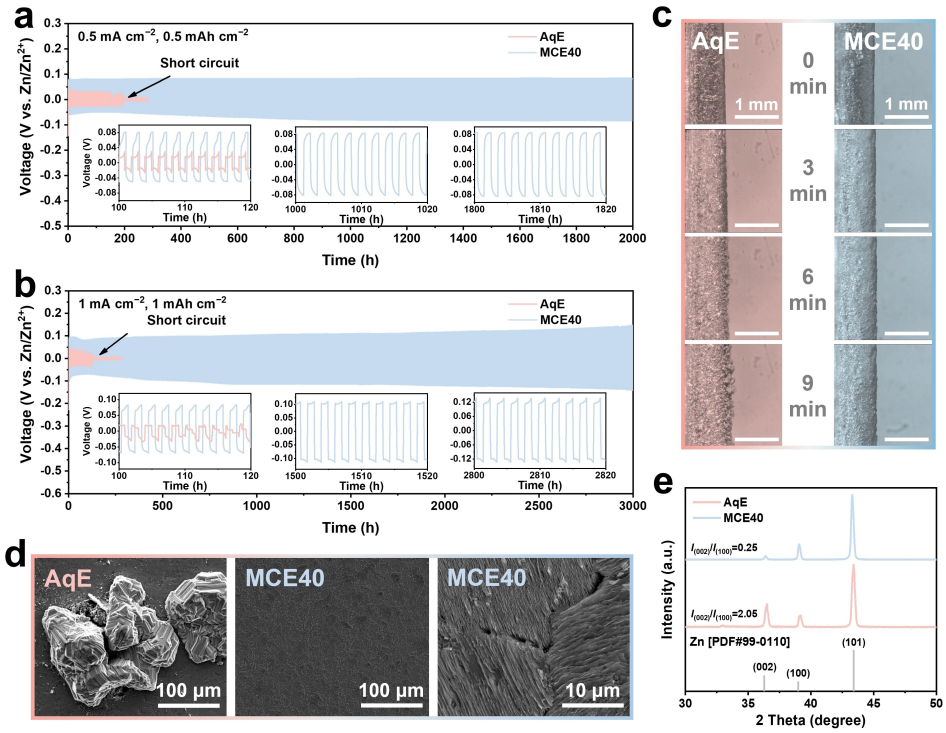

Figure 3. Electrochemical performance of AqE and MCE40 in Zn/Zn symmetric cells. Cycling performance of Zn/Zn symmetric cells under (a) current density of 0.5 mA cm^{-2} to 0.5 mAh cm^{-2} and (b) current density of 1.0 mA cm^{-2} to 1.0 mAh cm^{-2}. (c) Optical Zn/Zn symmetric cells under a current density of 2.0 mA cm^{-2}. (d) SEM images and (e) XRD patterns of the Zn electrodes cycled under 1.0 mA cm^{-2} to 1.0 mAh cm^{-2} for 20 cycles.

Zn-deposited Cu foils, Zn foil cycled in MCE40 primarily displays the (100) and (101) facets with an intensity ratio of only 0.25 between (002) and (100) facets, while Zn foil in AqE exhibits intense signals of all three planes with a ratio for $I_{(002)}/I_{(100)}$ of 2.05. The hexagonal flake-shaped Zn metal crystal unit has (100) and (101) planes as its side faces (Figure S25). When Zn crystals tend to deposit vertically, the (100) and (101) planes will be dominant in the deposited Zn. Therefore, the vertically packed Zn in the SEM image correlates to the strong peaks of (100) and (101) facets in the XRD pattern. Moreover, MCE40 effectively mitigated side reactions during cycling. As depicted in Figure S26, the battery in AqE experienced noticeable expansion due to the generation of hydrogen and oxygen gases during cycling, whereas the thickness of the battery in MCE40 remained nearly unchanged. The occurrence of the HER is further supported by XRD patterns between 5 to 20°, revealing the formation of $Zn_5(OH)_8Cl_2{\cdot}H_2O$, a byproduct of the HER, on the Zn electrode cycled in AqE (Figure S27). Furthermore, the higher corrosion potential and lower corrosion current observed for MCE40 in the Tafel plots of Zn/Zn symmetric cells indicate its favorable anti-corrosion capability (Figure S28).

In addition, enhanced Zn plating/stripping kinetics in MCE40 was revealed through a series of electrochemical tests. The charge transfer activation energy on the electrode surface was determined using the electrochemical impedance spectroscopy (EIS) results at various temperatures and the Arrhenius equation. Figure S29 demonstrates that MCE40 facilitates Zn^{2+} ion transport and Zn deposition. The reduced activation energy in MCE40 can be ascribed to its high Zn^{2+} ion transference number. Additionally, the Tafel slope values obtained from LSV measurements indicate a low Tafel slope for MCE40, suggesting improved Zn/Zn^{2+} redox reaction kinetics (Figure S30). The rapid Zn plating/stripping kinetics was also confirmed by the exchange current densities derived from Zn/Zn symmetric cells cycled at different rates to achieve 1.0 $mAh\,cm^{-2}$ (Figure S31a). Figure S31b exhibits a higher exchange current density in MCE40 than AqE, representing boosted reaction kinetics at the electrode surface. Notably, the overpotentials of the batteries in MCE40 are larger than those in AqE at different current densities, representing poor kinetics in MCE40, which seems to conflict with the above reaction kinetics results. However, it should be emphasized that mass transfer plays a key role in the overpotential of MCE40. Since there is no mass transfer limitation within AqE, the overpotential is only determined by charge-transfer resistance. In contrast, additional mass-transfer resistance contributes to the overpotential in MCE40.[10] Therefore, the overpotentials in MCE40 are larger than AqE, whereas the reaction kinetics in MCE40 is boosted.

Morphology and Crystallography Evolution During Zn Deposition

In the previously discussed results regarding Zn deposited Zn foils and Cu foils, the (002) facets were suppressed in the MCE40, whereas AqE maintains all three main crystalline planes. To analyze the reason for the different morphologies and crystallography of Zn deposition in both electrolytes, ex situ SEM and XRD analyses were conducted on Zn and Cu foils subjected to Zn deposition for varying times. As depicted in Figure 4a, after depositing for 20 minutes in AqE, a noticeable aggregation of Zn on limited spots can be found, indicative of the early state of Zn dendrite formation. After 40 minutes of deposition, large islands comprising Zn dendrites with uncovered Zn substrate become apparent in the SEM image. Subsequently, after 60 and 80 minutes, the Zn islands gradually merge together, forming a nonuniform surface with some Zn dendrites and vacancies. It is noteworthy that all these features are observed under a scale bar of 200 μm, indicating the substantial size of unfavorable Zn dendrites and islands. In contrast, under a zoomed-in view with a scale bar of 10 μm, the behavior of Zn deposition in MCE40 differs significantly from that in AqE. Figure 4b demonstrates that deposited Zn tends to form small Zn grains with an average diameter of around 2 μm. These Zn grains exhibit a nanosheet/nanosphere-like morphology with vertically arranged structures. With an increase in deposition time to 20 minutes, the growth of Zn grains with more evident nanosheet-like features becomes apparent. After 30 minutes of deposition, the size of Zn nanospheres remains relatively unchanged, whereas the arrangement of these Zn grains becomes denser compared to that observed after 20 minutes. Following a 40-minute deposition, the SEM image reveals a dominance of more densely arranged Zn grains with almost unaltered size. After depositing for 50 minutes, those small Zn grains merge to form Zn coral structures, with observable gaps between each grain. Over the next 10 minutes, the merging of Zn grains becomes more pronounced, accompanied by a decrease in the gaps between them. By the 70-minute mark, the merging of Zn grains results in a flat and uniform surface with fewer features resembling Zn nanospheres and gaps. Finally, after 80 minutes, the merging process is complete, presenting a uniform surface with vertically arranged Zn, akin to the features observed on the Zn foil from Zn/Zn symmetric cells. A similar characteristic is also noticeable at the interface between the electrolyte and the atmosphere (Figure S32).

The gradual evolution of Zn morphology and crystallography unveils the reason for the exposure of (100) and (101) planes. Considering the instability of a single Zn crystal growing along [100] and [101] directions, Zn crystals tend to deposit as small grains, which offer higher stability. During the subsequent deposition process, adjacent Zn grains gradually grow bigger and merge together, providing mutual support until dense deposition occurs. This nucleation-merge-growth mechanism circumvents the unfavorable features and tip effect of the growth along [100] and [101] directions, allowing Zn deposition along vertical crystalline directions to maintain a dense and uniform morphology.

XRD measurements were conducted on the Cu electrodes after deposition at different times to confirm the change in crystallinity during deposition. As shown in Figure 4c, with the increase in deposition time, the peak intensity of the (002) facet gradually increases on the Cu foil cycled in

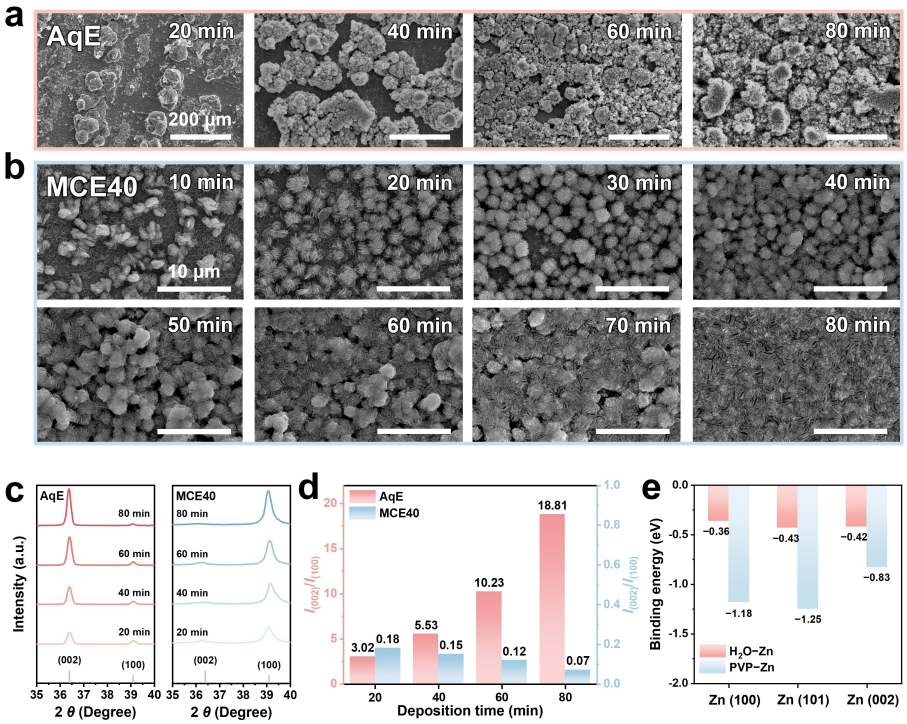

Figure 4. Characterizations of Zn deposited Zn and Cu foils after different depositing times. SEM images of Zn deposited Zn foils within (a) AqE and (b) MCE40. (c) XRD patterns of Zn deposited Cu foils after different times, and (d) corresponding statistical results of intensity ratio between (002) and (100) facets. (e) Adsorption energies of H_2O and PVP on three facets derived from DFT calculations.

AqE. In contrast, the peak intensity of the (100) facet exhibits an obvious increase after 80 minutes in MCE40. Statistical analysis demonstrates that the (002) facet predominates in the deposited Zn in AqE, while the (002) planes are scarcely found on the Cu foil in MCE40, indicating the exposure of the (002) facet has been suppressed due to the existence of PVP in the electrolyte (Figure 4d).

In addition to characterizing the deposited electrodes at different times, Zn deposition on Cu foils was also measured under various current densities to a capacity of 5.0 $mAh\,cm^{-2}$ (Figure S33). In the case of AqE, with the increase of current densities, the peak intensity ratios between (002) and (100) facets remain very similar without significant change. The crystallography of deposited Zn is closely tied to the kinetics of Zn deposition.[24] All three facets can be activated at these elevated current densities, resulting in the same depositing rate across all facets. In contrast, significant differences are noted in the peak intensity ratio between (002) and (100) facets in MCE40 under varying current densities. The suppression of the (002) facet with the increase of current density can be ascribed to the enhanced difference in the deposition kinetics for each facet as the current density rises. This alternation in deposition kinetics across all three facets may stem from the differential adsorption abilities of PVP molecules on each crystalline plane.

PVP molecules are extensively utilized in nanoparticle synthesis due to their ability to adsorb on specific crystalline facets of nanoparticles.[25] This adsorption prevents further growth on these facets and promotes the preferential development of other crystalline planes.[26] Furthermore, PVP molecules have been employed to modify the morphology and active sites for cathode materials of AZMBs due to their specific adsorption properties.[27] Accordingly, the adsorption capabilities of PVP and H_2O molecules on the Zn metal substrate were evaluated using DFT calculations (Figure S34). As illustrated in Figure 4e, compared to the relatively modest adsorption energies associated with H_2O molecules, PVP molecules exhibit significantly higher adsorption energies on all examined facets. This suggests a pronounced tendency for PVP to adsorb to the Zn surface rather than H_2O molecules. Notably, the adsorption energy of PVP molecules on the (002) facet is lower than that on the other two facets, indicating preferential adsorption of PVP molecules on the (100) and (101) facets over the (002) plane. This differential adsorption pattern promotes the enhanced growth of the (002) facet, resulting in the exposure of the (100) and (101) features, aligning with the previous XRD and SEM results in MCE40. In contrast, without the PVP-mediated preferential deposition, the (002) facet, which possesses the lowest surface energy, becomes predominantly exposed, correlating to the results in AqE.

It is noteworthy that although widely accepted theories attribute the preferential facet growth to the specific adsorption of introduced molecules, previous works employing PVP as additives to the electrolyte did not report a similar dense and vertical morphology as this work.[15] In contrast, flat and plate-like Zn can be observed on the deposited electrodes, corresponding to the (002) texture.

Therefore, the preferential zinc deposition with (100) and (101) facets might be intricately linked to the reactions occurring at the electrode-electrolyte interface. To better evaluate the electrochemical reactions at this interface, an experimental setup employing a three-electrode system was utilized. This system comprised a glassy carbon-based RDE as the working electrode, a Zn foil as the counter electrode, and an Ag/AgCl electrode (sat. KCl) as the reference electrode. LSV measurements were employed to measure the current-potential curves in both AqE and MCE40. In the absence of rotation applied to the RDE working electrode, the *i-t* curves manifest distinct behaviors in both electrolytes. Within the potential range of −1.0 and −1.8 V, the curve of AqE shows a linear ohmic relationship, indicating that the mass transfer at the electrode surface is rapid enough to offset the consumption of Zn^{2+} by redox reactions (Figure 5a). However, beyond −1.8 V, a slope decrease can be observed, indicative of a reduction of ionic conductivity caused by Zn^{2+} depletion. Subsequently, an increase in the slope of the curve is noted, which correlates to the start of other alternative mechanisms that facilitate mass transfer to counteract ion depletion. Even though the curve of MCE40 exhibits a similar shape to the one for AqE, a more obvious slope change due to more severe mass transfer limitation is evident (Figure 5d). This is followed by the initiation of electroconvection, leading to another linear ohmic region. The prolonged ion depletion can be attributed to the elevated viscosity and reduced ionic conductivity in MCE40, which impedes the diffusion of Zn^{2+} towards the electrode surface. The impact of mass transfer limitation on the current response was confirmed by the LSV tests with RDE under rotation. As shown in Figure 5a, the application of rotation on the electrode results in a curve that exhibits a linear ohmic relationship throughout, without any limitation region. In the curve for MCE40, despite the observable slope change, the overall curve closely approximates a linear relationship (Figure 5d). Considering the critical role of ion diffusion from the electrolyte to the electrode in Zn deposition, the big difference in the LSV curves indicates that the mass transfer-governed ion diffusion in the electrolyte would influence the Zn deposition dynamics.

CA measurements were conducted under an overpotential of −2.2 V to assess the impact of mass transfer limitation on Zn deposition, aligning with the potential within the over-limiting region. In the AqE without RDE rotation, a current decrease can be observed before Sand's time (t_{Sand}), coupled with a continuous current increment after t_{Sand} (Figure 5b).[28] The lowest current indicates the establishment of a Zn^{2+} ion depletion layer, denoting complete consumption of Zn^{2+} ions. The subsequent current elevation after t_{Sand} represents the initiation of the additional mass transfer mechanism.[12,29] However, unlike showing t_{Sand} in AqE, the current in MCE40 demonstrates a consistent decline over 60 seconds, demonstrating the absence of

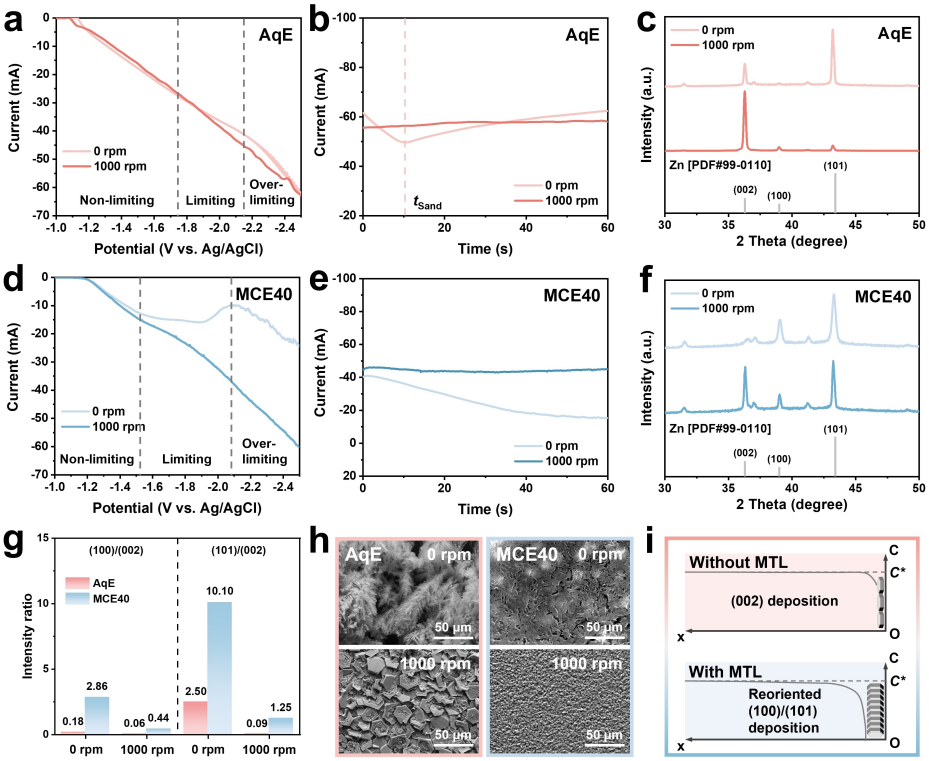

Figure 5. Electrochemical tests and characterization results of the RDEs in three-electrode systems. (a) LSV curves, (b) *i-t* curves from CA measurement of Zn deposition on RDEs in AqE, and (c) corresponding XRD patterns. (d) LSV curves, (e) *i-t* curves from CA measurement of Zn deposition on RDEs in MCE40, and (f) corresponding XRD patterns. (g) Peak intensity ratio of (100)/(002) and (101)/(002) deduced from (c) and (f). (h) SEM images of Zn deposited RDEs with and without rotation in both electrolytes. (i) Illustration of the relationships between crystallography of Zn deposition and concentration near the electrode with and without mass transfer limitation (MTL).

electroconvection after the depletion of Zn^{2+} near the electrode surface (Figure 5e). Consequently, Zn^{2+} ions outside of the depletion layer cannot supply Zn^{2+} to the electrode, resulting in continuous current reduction. These CA results highlight a more pronounced mass transfer limitation within the MCE40 and a more challenging start for alternative mass transfer mechanisms. In contrast, by applying rotation to the RDE to facilitate mass transfer, the currents in both electrolytes are maintained at their initial values without any decrease, suggesting that mass transfer limitations were mitigated in both electrolytes.

To elucidate the effect of mass transfer limitation on the crystallography of Zn deposition, the RDEs with and without rotation after CA measurements were analyzed using SEM and XRD. Figure 5c illustrates that the deposited Zn in the AqE predominantly comprises the (002) and (101) facets in the absence of rotation. However, upon negating mass transfer limitation through rotating RDE, the XRD pattern distinctly emphasizes the (002) plane, corresponding to the results from prior studies.[12] In contrast, under severe mass transfer limitation in the MCE40, the (002) facet is scarcely visible on the non-rotated RDE (Figure 5f). Similar to the observation in the AqE, applying rotation to the RDE in the MCE40 yields a more pronounced presence of the (002) facet in the XRD pattern, suggesting that an ample supply of Zn^{2+} ions on the electrode surface promotes the planar deposition of the (002) facet. In contrast to the result in AqE where the (101) facet nearly vanishes, the (101) plane remains observable in MCE40. This persistence can be ascribed to the influence of adsorbed PVP molecules on the electrode surface, which regulate the deposition of the (101) facet. Statistical analysis summarizes the variations in crystallography across both electrolytes with and without mass transfer limitation. As shown in Figure 5g, without the rotation, both electrolytes predominantly exhibit the (101) facet. This trend is particularly pronounced in MCE40, which experiences more significant mass transfer limitations. With the application of rotation to the RDE, the ratios of (100)/(002) and (101)/(002) decrease for both electrolytes, indicating a promoted formation of the (002) facet consequent to the mitigation of mass transfer limitation. It is noteworthy that, even under rotation conditions, the diffraction peaks corresponding to (100) and (101) facets of Zn deposited in MCE40 maintain high intensity, likely due to the adsorbed PVP molecules. Therefore, the specific adsorption of PVP molecules on the Zn foil, coupled with the mass transfer limitation in the electrolyte close to the electrode, simultaneously inhibits the exposure of the (002) facet while facilitating the visibility of the (100) and (101) planes.

CA measurements were conducted at the non-limiting region (−1.3 V) to evaluate the combined effects of PVP adsorption and mass transfer limitation. At this potential, mass transfer limitations are negligible in both electrolytes, leading to an absence in the current reduction (Figure S35a and S35b), similar to the results with rotating RDEs observed in Figure 5b and 5e. Consequently, the (002) facet becomes prominent in the XRD patterns of Zn metal deposited in AqE (Figure S35c). This predominance mirrors the findings under rotational conditions in Figure 5c, which is attributed to the alleviation of the mass transfer limitation. However, the XRD patterns for Zn metal deposited under −1.3 V in MCE40 exhibit a more obvious intensity of the (002) facet compared to conditions with mass transfer limitations shown in Figure 5f, indicating that the absence of a mass transfer limitation in the electrolyte can facilitate the exposure of the (002) facet (Figure S35d). Furthermore, the adsorption of PVP molecules on the electrode surface results in more intense peaks for the (100) and (101) facets in MCE40 compared to AqE, highlighting the role of PVP adsorption. Therefore, under the simultaneous regulation of PVP adsorption and mass transfer limitation, the presence of the (002) facet in MCE40 was significantly reduced. Notably, the intensity ratios of $I_{(100)}/I_{(002)}$ and $I_{(101)}/I_{(002)}$ under −2.3 V in the over-limiting region drastically decreased when rotation was applied, which is due to the alleviation of mass transfer limitation (Figure 5g). In contrast, these intensity ratios under −1.3 V in the non-limiting region barely changed when the rotation of RDEs was applied (Figure S36). These results confirm that the exposure of the (002) facet is highly related to a mass transfer limitation.

The morphological difference of deposited Zn under varying conditions in both electrolytes within the over-limiting region (−2.3 V) is more distinctly visualized through SEM images. As shown in Figure 5h, without rotation, deposited Zn in AqE manifests classical tree-like dendritic structures. In contrast, within MCE40, a dense and vertically arranged Zn morphology is observed, which is caused by the mass transfer limitation and the adsorption of PVP on the electrode surface. This vertical deposition pattern is also corroborated by the XRD results presented in Figure 5f. Upon the application of rotation, Zn deposition on the electrode surface in the AqE transitions to a characteristic and typical hexagonal-like morphology, reflecting the dominance of the (002) facet as indicated in the XRD results. This observation confirms that alleviating the mass transfer limitation promotes the preferential deposition of the (002) plane. Meanwhile, to mitigate the impact of electrolyte flow on the deposition morphology and crystalline orientation during rotation in AqE, the CA measurement was conducted without rotating the RDE, followed by a sixty-second rotation of the RDE under 1000 rpm. The SEM image of the Zn-deposited RDE revealed dendrite-like features, demonstrating that the electrolyte flow exerts minimal influence on the deposition morphology (Figure S37). Moreover, the application of rotation leads to the disappearance of the vertical Zn deposition in MCE40, underscoring the critical impact of mass transfer limitation in influencing the exposure of (100) and (101) facets (Figure 5h).

In summary, the orientation and morphology of Zn deposition are significantly influenced by the presence of a mass transfer limitation at the electrode surface (Figure 5i). In conditions where mass transfer limitations are absent, Zn preferentially exposes (002) texture due to the low surface energy of the (002) facet and sufficient Zn^{2+} supply, resulting in a flat and uniform Zn deposition. When the mass transfer limitations are partially present, as observed in AqE, the (002) plane initially deposits preferentially on the

substrate until the consumption of Zn^{2+} ions approaches completion near the electrode surface. Following this, deposition begins to occur along the [100] and [101] orientations, culminating in a deposition profile that incorporates all three main facets. When the mass transfer limitation is pronounced, such as in MCE40, a Zn^{2+} depletion layer appears rapidly, hindering the exposure of the (002) facet. This triggers a reorientation of crystallography, during which the (100) and (101) facets start to mitigate the mass transfer limitation by accessing Zn^{2+} from the electrolyte beyond the depletion layer. Consequently, with the aid of the "nucleation-merge-growth" mechanism, Zn gains with (100) and (101) textures merge with each other and grow into a closely packed and vertically arranged morphology.

Electrochemical Performance of MCE40 in Full Cell Batteries

To further explore the practicality of MCE40, NaVO and MnO_2 were utilized as cathode materials to assemble NaVO/Zn and MnO_2/Zn full cell batteries, respectively. The morphologies shown via SEM and XRD patterns of the as-prepared NaVO and MnO_2 are consistent with those reported in previous literature (Figure S38).[30] The CV profiles of NaVO/Zn batteries in both AqE and MCE40 revealed similar redox peaks and exhibited high reversibility, indicating that the processes for cation intercalation/deintercalation are highly reversible (Figure S39). However, more redox peaks were discernible between 0.4–0.8 V in AqE during both cathodic and anodic sweeps in the initial cycle, which can be attributed to the insertion of H^+ into the cathode materials (Figure S40). In contrast, the lower water activity in MCE40 diminished the activity of protons, leading to a reduction of redox peaks observed within MCE40. Despite the observation of an increased number of redox reactions in AqE, which initially suggests a higher capacity during cycling, the cycling performance of NaVO/Zn battery in AqE significantly underperforms compared to that in MCE40. As shown in Figure 6a, while NaVO/Zn in AqE exhibits higher initial capacity at 1.0 A g^{-1}, it undergoes rapid capacity degradation, retaining merely 16 % of its initial capacity after 500 cycles. In contrast, the NaVO/Zn battery cycled in MCE40 displays remarkable endurance, maintaining 80 % of its initial capacity over the same number of cycles under identical conditions. This enhanced capacity retention and superior cycling stability in MCE40 can be ascribed to the formation of a dendrite-free Zn anode, coupled with mitigated dissolution of cathode materials facilitated by the reduced water activity within the MCE40. This trend is consistent across variable rate cycling tests (Figure 6b). Even though the capacities at rates

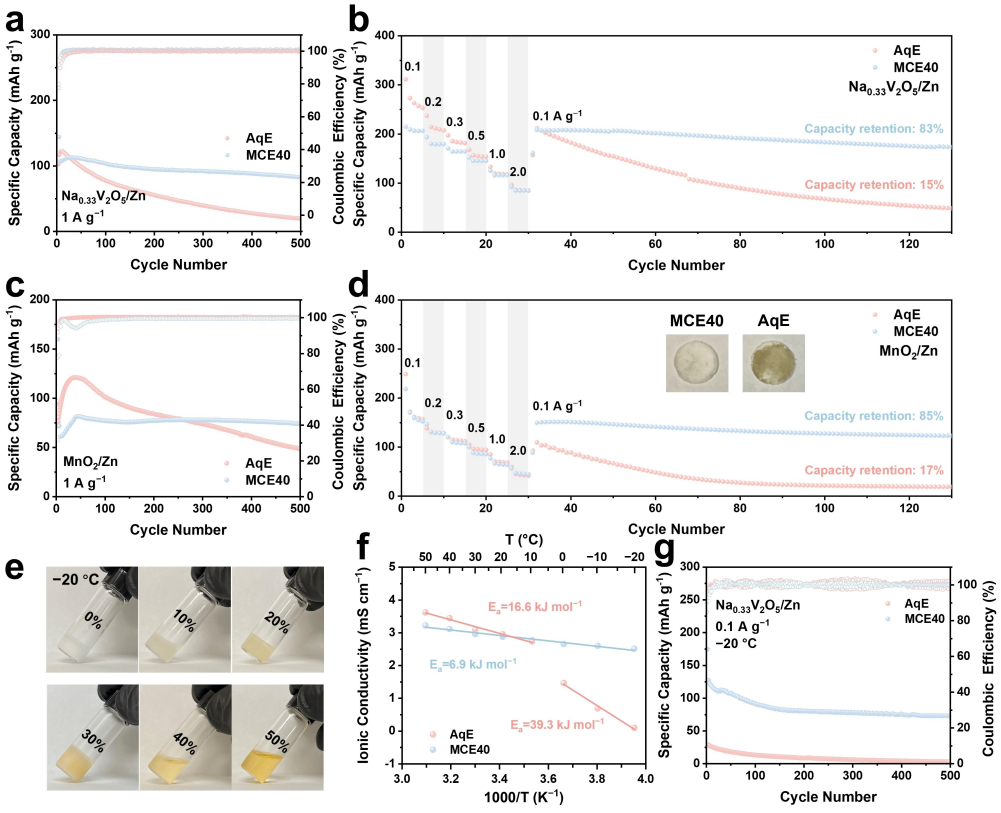

Figure 6. Electrochemical performance of NaVO/Zn and MnO_2/Zn full cell batteries in both electrolytes. Cycling performance of NaVO/Zn under (a) 1.0 A g^{-1} and (b) variable rates. Cycling performance of MnO_2/Zn under (c) 1.0 A g^{-1} and (d) variable rates. (e) Digital photos of AqE and MCEs under −20 °C. (f) Ionic conductivity and corresponding Arrhenius plots for calculating conductive activation energy. (g) Cycling performance of NaVO/Zn at 0.1 A g^{-1} at −20 °C in both electrolytes.

between 0.1 to 0.5 $A g^{-1}$ are initially higher in AqE, which is due to the additional intercalation of protons in the cathode materials, an obvious capacity decay is observed, eventually equating the performance to that of MCE40 at rates of 1.0 and 2.0 $A g^{-1}$. Furthermore, the recovered capacities at 0.1 $A g^{-1}$ in both electrolytes show a similar value, indicating the dissolution on the cathode and side reactions on the anode deteriorate the electrochemical reversibility and stability of the NaVO/Zn battery in AqE. After an additional 100 cycles at 0.1 $A g^{-1}$, the NaVO/Zn battery in MCE40 exhibits a capacity retention of 83 %, while its counterpart in AqE suffers a drastic drop, preserving only 15 % of its original capacity. Moreover, the galvanostatic charge–discharge (GCD) curves across various current densities reveal higher polarization in AqE, culminating in diminished capacities (Figure S41).

The MnO_2/Zn batteries cycled in MCE40 also demonstrate favorable stability and capacity. As shown in Figure 6c, the presence of a substantial quantity of free water in AqE enables the MnO_2/Zn battery to provide higher initial capacity than in MCE40, accompanied by a capacity activation process. However, a significant capacity decay appears after 50 cycles, with only 16 % of the initial capacity being retained after 500 cycles. In contrast, although the initial capacity of the MnO_2/Zn battery in MCE40 is lower than that in AqE, it exhibits remarkable cycling stability for over 500 cycles with a capacity retention of 92 %, demonstrating the superior sustainability and effectiveness of MCE40 in supporting the long-term cycling performance of full cell batteries. The MnO_2/Zn battery in MCE40 also performs stably in variable rate cycling tests. Figure 6d illustrates that starting from a current density of 0.1 $A g^{-1}$, the capacity observed in AqE is initially comparable to that in MCE40 without an activation process. The capacities of the MnO_2/Zn batteries in both electrolytes remain closely matched until the cycling rate returns to the recovered rate of 0.1 $A g^{-1}$. Subsequently, capacity retention in AqE dramatically falls to 17 % after another 100 cycles, whereas in MCE40, an impressive 85 % of capacity is maintained after the same number of cycles. The disparity in cycling performance between the electrolytes can be attributed not only to the favorable Zn deposition on the anode side but also to the inhibited dissolution of MnO_2 on the cathode side in MCE40. Further evidence supporting this observation is provided by the inset images in Figure 6d, where the separator from the battery cycled in AqE shows a dark brown color, indicative of the dissolution of MnO_2 cathode materials into the electrolyte, while the separator from the battery cycled in MCE40 still retains its original white color, confirming the effective suppression of cathodic dissolution in this system.

Since the incorporation of PVP significantly alters the hydrogen bonding environment, anti-freezing properties were also investigated. To examine the anti-freezing capabilities, different electrolytes were subjected to a temperature of −20 °C for 5 hours. AqE and MCEs10-30 underwent solidification under these conditions, while MCE40 and 50 still maintained a liquid phase without ice formation, indicating that a PVP content above 40 % effectively prevents the electrolyte from freezing (Figure 6e). Differential scanning calorimetry (DSC) results, as depicted in Figure S42, indicate a shift in freezing points towards more negative temperatures with increasing PVP content. Notably, the absence of freezing peaks for MCE40 and MCE50 within the examined temperature range suggests freezing points lower than −80 °C. Ionic conductivities at varying temperatures for AqE and MCE40 were determined from the EIS results (Figure S43). Figure S44 shows an apparent reduction in ionic conductivity when the temperature is below 0 °C, highlighting the adverse effect of low temperatures on ion diffusion within AqE. The activation energy (E_a) for ionic conduction was calculated based on the Arrhenius relationship. As described in Figure 6f, AqE exhibits two distinct activation energies: 16.6 $kJ mol^{-1}$ at temperatures above 0 °C and 39.3 $kJ mol^{-1}$ below 0 °C. However, MCE40 maintains a constant E_a across all temperatures. The elevated E_a suggests that ionic conductivity in AqE is more sensitive to temperature changes compared to MCE40, leading to its solidification at −20 °C.

The electrochemical performance of AqE and MCE under extreme temperatures (i.e., −20 and 50 °C) was evaluated in Zn/Cu half cells, Zn/Zn symmetric cells, and NaVO/Zn full cells. As illustrated in Figure S45, the Zn/Cu half cells in MCE40 exhibit commendable CEs at both −20 and 50 °C. In contrast, the reduced ionic conductivity and parasitic reactions at these temperatures deteriorate the reversibility of Zn plating/stripping in AqE. Furthermore, the sluggish ionic diffusion and plating kinetics on the electrode surface in AqE lead to a short circuit in Zn/Zn symmetric cells after 20 hours (Figure S46a). However, a symmetric cell with MCE40 achieves stable cycling for over 500 hours without failure or any polarization, showcasing its resilience under low-temperature conditions (Figure S47). This favorable cycling performance of the Zn/Zn symmetric cell in MCE40 is also observed at 50 °C, in contrast to the significant polarization and rampant dendrite formation in cells using AqE (Figure S46b). In the case of NaVO/Zn full cells at −20 °C, batteries using AqE exhibit a capacity decay at −20 °C, eventually decreasing to almost 0 $mAh g^{-1}$, while the NaVO/Zn cells in MCE40 maintain stable cycling for over 500 cycles with capacities comparable to those achieved at room temperature (Figure 6g). This indicates that the ion transport in MCE40 is minimally affected by the low temperature. Furthermore, at the elevated temperature of 50 °C, batteries employing AqE experience a quick capacity fading within the first 30 cycles, attributed to accelerated dissolution kinetics at the cathode (Figure S48). In contrast, the NaVO/Zn battery within MCE40 demonstrates stable cycling for more than 400 cycles with a capacity retention of 71 %, underscoring the enhanced thermal stability and electrochemical performance afforded by MCE40 under extreme temperature conditions.

Conclusion

In summary, this work introduced a macromolecular crowding electrolyte created by incorporating PVP into aqueous

electrolytes, promoting an enlarged electrochemical window and uniform Zn deposition. Characterizations through ex situ SEM and XRD revealed the "nucleation-merge-growth" process, resulting in closely-packed and vertically-aligned Zn deposited prominently featuring the (100) and (101) crystalline facets. Furthermore, the CA measurements, coupled with subsequent SEM and XRD analyses, highlighted that the mass transfer limitation within the MCE40 caused the reorientation of the crystalline structure by suppressing the exposure of the (002) plane. Meanwhile, the DFT results indicated that the specific adsorption of PVP molecules on the Zn electrode surface encourages preferential growth along [002] direction, thereby eventually exposing the (100) and (101) facets. Governed by uniformly deposited Zn and compact structure caused by mass transfer limitation and "nucleation-merge-growth" mechanism, the MCE40 facilitated highly reversible Zn plating/stripping in Zn/Cu half cells over 600 cycles with an average CE of 99.4 %, and demonstrated extended durability in Zn/Zn symmetric cells for over 3000 hours. Furthermore, the NaVO/Zn and MnO_2/Zn full cells showed promising specific capacity and sustained stability at both room and sub-zero temperatures. This study underscores a new mechanism for controlling crystallographic orientation for preferential Zn deposition, offering a fresh perspective on fabricating sustainable Zn anodes for aqueous zinc metal batteries.

Acknowledgements

The authors gratefully acknowledge the Welch Foundation for their generous support through Grant F-1841 (G. H.). This research was partially supported by the National Science Foundation (NSF) (CHE-2102317, CHE-2109120, and DMS1929348). The authors gratefully acknowledge the Center for Electrochemistry, University of Texas at Austin, for providing partial financial support for this work through the CEC Student Scholar Fellowship (Z. W.) under Grant no. H-F-0037 from the Welch Foundation.

Conflict of Interest

The authors declare no conflict of interest.

Data Availability Statement

The data that support the findings of this study are available from the corresponding author upon reasonable request.

Keywords: mass transfer limitation · preferential Zn deposition · molecular crowding electrolyte · low-temperature electrolyte · Zn anode

[1] a) Y. Liu, X. Lu, F. Lai, T. Liu, P. R. Shearing, I. P. Parkin, G. He, D. J. L. Brett, *Joule* **2021**, *5*, 2845–2903; b) S. Liu, R. Zhang, C. Wang, J. Mao, D. Chao, C. Zhang, S. Zhang, Z. Guo, *Angew. Chem. Int. Ed.* **2024**, *63*, e202400045; c) P. Ruan, S. Liang, B. Lu, H. J. Fan, J. Zhou, *Angew. Chem. Int. Ed.* **2022**, *61*, e202200598; d) G. Fang, J. Zhou, A. Pan, S. Liang, *ACS Energy Lett.* **2018**, *3*, 2480–2501.

[2] a) K. Roy, A. Rana, J. N. Heil, B. M. Tackett, J. E. Dick, *Angew. Chem. Int. Ed.* **2024**, *63*, e202319010; b) Y. Dai, C. Zhang, J. Li, X. Gao, P. Hu, C. Ye, H. He, J. Zhu, W. Zhang, R. Chen, W. Zong, F. Guo, I. P. Parkin, D. J. L. Brett, P. R. Shearing, L. Mai, G. He, *Adv. Mater.* **2024**, 2310645.

[3] a) Q. Zhang, J. Luan, Y. Tang, X. Ji, H. Wang, *Angew. Chem. Int. Ed.* **2020**, *59*, 13180–13191; b) X. Yu, Z. Li, X. Wu, H. Zhang, Q. Zhao, H. Liang, H. Wang, D. Chao, F. Wang, Y. Qiao, H. Zhou, S.-G. Sun, *Joule* **2023**, *7*, 1145–1175; c) Y. Zhang, H. Dong, R. Yang, H. He, G. He, F. Cegla, *Electrochem. Commun.* **2024**, *162*, 107700.

[4] a) J. Feng, X. Li, X. Cui, H. Zhao, K. Xi, S. Ding, *Adv. Energy Mater.* **2023**, *13*, 2204092; b) Z. Shi, M. Yang, Y. Ren, Y. Wang, J. Guo, J. Yin, F. Lai, W. Zhang, S. Chen, H. N. Alshareef, T. Liu, *ACS Nano* **2023**, *17*, 21893–21904; c) W. Yuan, X. Nie, Y. Wang, X. Li, G. Ma, Y. Wang, S. Shen, N. Zhang, *ACS Nano* **2023**, *17*, 23861–23871; d) Z. Huang, Z. Li, Y. Wang, J. Cong, X. Wu, X. Song, Y. Ma, H. Xiang, Y. Huang, *ACS Energy Lett.* **2023**, *8*, 372–380; e) C. Yang, P. Woottapanit, Y. Yue, S. Geng, J. Cao, X. Zhang, G. He, J. Qin, *Small* **2024**, 2311203.

[5] a) M. Wang, J. Ma, Y. Meng, J. Sun, Y. Yuan, M. Chuai, N. Chen, Y. Xu, X. Zheng, Z. Li, W. Chen, *Angew. Chem. Int. Ed.* **2023**, *62*, e202214966; b) Z. Zhao, R. Wang, C. Peng, W. Chen, T. Wu, B. Hu, W. Weng, Y. Yao, J. Zeng, Z. Chen, P. Liu, Y. Liu, G. Li, J. Guo, H. Lu, Z. Guo, *Nat. Commun.* **2021**, *12*, 6606; c) Q. He, Z. Chang, Y. Zhong, S. Chai, C. Fu, S. Liang, G. Fang, A. Pan, *ACS Energy Lett.* **2023**, *8*, 5253–5263.

[6] Y. Wang, L. e Mo, X. Zhang, Y. Ren, T. Wei, Z. Li, Y. Huang, H. Zhang, G. Cao, L. Hu, *Adv. Energy Mater.* **2023**, *13*, 2301517.

[7] K. E. K. Sun, T. K. A. Hoang, T. N. L. Doan, Y. Yu, X. Zhu, Y. Tian, P. Chen, *ACS Appl. Mater. Interfaces* **2017**, *9*, 9681–9687.

[8] Z. Liu, Z. Guo, L. Fan, C. Zhao, A. Chen, M. Wang, M. Li, X. Lu, J. Zhang, Y. Zhang, N. Zhang, *Adv. Mater.* **2024**, *36*, 2305988.

[9] Q. Zhu, G. Sun, S. Qiao, D. Wang, Z. Cui, W. Zhang, J. Liu, *Adv. Mater.* **2024**, *36*, 2308577.

[10] A. J. Bard, L. R. Faulkner, H. S. White, *Electrochemical methods: fundamentals and applications*, John Wiley & Sons **2022**.

[11] N. Li, J. Wang, Q. Zhang, X. Zhou, H. Wang, G. Lu, J. Zhao, Z. Chen, G. Cui, *Batteries & Supercaps* **2023**, *6*, e202300058.

[12] J. Zheng, J. Yin, D. Zhang, G. Li, D. C. Bock, T. Tang, Q. Zhao, X. Liu, A. Warren, Y. Deng, S. Jin, A. C. Marschilok, E. S. Takeuchi, K. J. Takeuchi, C. D. Rahn, L. A. Archer, *Sci. Adv.* **2020**, *6*, eabb1122.

[13] R. J. Ellis, *Trends Biochem. Sci.* **2001**, *26*, 597–604.

[14] F. Haaf, A. Sanner, F. Straub, *Polym. J.* **1985**, *17*, 143–152.

[15] a) S. Gao, J. Han, Z. Liu, K. Wang, K. Jiang, C. Guo, Y. Tan, D. Zhou, W. Shi, *J. Electrochem. Soc.* **2021**, *168*, 080514; b) C. Lin, Y. Liu, X. Zhang, X. Miao, Y. Chen, S. Chen, Y. Zhang, *J. Power Sources* **2022**, *549*, 232078.

[16] E. Stefanutti, L. E. Bove, F. G. Alabarse, G. Lelong, F. Bruni, M. A. Ricci, *J. Chem. Phys.* **2019**, *150*.

[17] Y. Guo, J. Gu, R. Zhang, S. Zhang, Z. Li, Y. Zhao, Z. Huang, J. Fan, Z. Chen, C. Zhi, *Adv. Energy Mater.* **2021**, *11*, 2101699.

[18] Y. Wang, T. Wang, D. Dong, J. Xie, Y. Guan, Y. Huang, J. Fan, Y.-C. Lu, *Matter* **2022**, *5*, 162–179.

[19] a) X. Zhao, X. Zhang, N. Dong, M. Yan, F. Zhang, K. Mochizuki, H. Pan, *Small* **2022**, *18*, 2200742; b) Q. Meng, Q. Bai, R. Zhao, P. Cao, G. Zhang, J. Wang, F. Su, X. Zhou, J. Yang, J. Tang, *Adv. Energy Mater.* **2023**, *13*, 2302828.

[20] W. Zhang, X. Wu, Q. Fu, H. Qu, J. Borowiec, M. Isaacs, G. Zhou, I. P. Parkin, G. He, *Chem. Commun.* **2023**, *59*, 13891–13894.
[21] Y. Zhao, S. Guo, M. Chen, B. Lu, X. Zhang, S. Liang, J. Zhou, *Nat. Commun.* **2023**, *14*, 7080.
[22] Z. Wang, J. Diao, G. Henkelman, C. B. Mullins, *Adv. Funct. Mater.* **2024**, *34*, 2314002.
[23] a) Z. Wang, D. Zhou, Z. Zhou, W. Gong, S. Zhao, Y. Ling, F. Liu, J. Guo, K. Zhao, J. Wu, P. Xue, C. Li, Y. Sun, J. Luo, Z. Wang, J. Xu, L. Wei, Q. Zhang, *Adv. Funct. Mater.* **2024**, 2313371; b) Z. Liu, R. Wang, Y. Gao, S. Zhang, J. Wan, J. Mao, L. Zhang, H. Li, J. Hao, G. Li, L. Zhang, C. Zhang, *Adv. Funct. Mater.* **2023**, *33*, 2308463.
[24] Z. Cai, J. Wang, Z. Lu, R. Zhan, Y. Ou, L. Wang, M. Dahbi, J. Alami, J. Lu, K. Amine, Y. Sun, *Angew. Chem. Int. Ed.* **2022**, *61*, e202116560.
[25] A. Kyrychenko, O. M. Korsun, I. I. Gubin, S. M. Kovalenko, O. N. Kalugin, *J. Phys. Chem. C* **2015**, *119*, 7888–7899.
[26] W. A. Al-Saidi, H. Feng, K. A. Fichthorn, *Nano Lett.* **2012**, *12*, 997–1001.
[27] a) S. Li, L. Qin, L. Li, H. Cheng, G. Fang, Q. Zhu, *Int. J. Electrochem. Sci.* **2021**, *16*, 210349; b) Y. Wang, M. Zhao, G. Gao, C. Zheng, D. He, C. Wang, G. Diao, *Small Methods* **2023**, *7*, 2300606.
[28] R. N. Wasalathanthri, R. Akolkar, *J. Electrochem. Soc.* **2022**, *169*, 092519.
[29] H. J. S. Sand, *The London, Edinburgh, and Dublin Philosophical Magazine and Journal of Science* **1901**, *1*, 45–79.
[30] a) Y. Hu, Z. Liu, L. Li, S. Guo, X. Xie, Z. Luo, G. Fang, S. Liang, *Natl. Sci. Rev.* **2023**, *10*; b) P. He, G. Zhang, X. Liao, M. Yan, X. Xu, Q. An, J. Liu, L. Mai, *Adv. Energy Mater.* **2018**, *8*, 1702463.

Manuscript received: April 25, 2024
Accepted manuscript online: June 3, 2024
Version of record online: ■■, ■■

Research Article

Zinc Batteries

Z. Wang, J. Wang, K. Kawashima, Z. Liu, G. Henkelman, C. B. Mullins* _____ e202407881

Mass Transfer Limitation within Molecular Crowding Electrolyte Reorienting (100) and (101) Texture for Dendrite-Free Zinc Metal Batteries

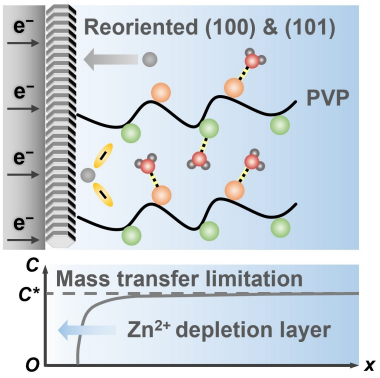

Polyvinylpyrrolidone (PVP) is introduced into $Zn(ClO_4)_2$ aqueous solution to prepare a macromolecular crowding electrolyte (MCE). Under the regulation of both specific adsorption of PVP on the Zn surface and mass transfer limitation in the MCE, the Zn deposition exhibits reoriented (100) and (101) textures. Consequently, MCE enables zinc metal batteries with dendrite-free deposition and high sustainability.